DOI 10.1103/physrevlett.120.204502
ISSN 0031-9007
ESSN 1079-7114

Regimes of Coriolis-Centrifugal Convection

Susanne Horn* and Jonathan M. Aurnou
Department of Earth, Planetary, and Space Sciences, University of California, Los Angeles, California 90095, USA

(Received 28 December 2017; published 15 May 2018)

Centrifugal buoyancy affects all rotating turbulent convection phenomena, but is conventionally ignored in rotating convection studies. Here, we include centrifugal buoyancy to investigate what we call Coriolis-centrifugal convection (C^3), characterizing two so far unexplored regimes, one where the flow is in quasicyclostrophic balance (QC regime) and another where the flow is in a triple balance between pressure gradient, Coriolis and centrifugal buoyancy forces (CC regime). The transition to centrifugally dominated dynamics occurs when the Froude number Fr equals the radius-to-height aspect ratio γ. Hence, turbulent convection experiments with small γ may encounter centrifugal effects at lower Fr than traditionally expected. Further, we show analytically that the direct effect of centrifugal buoyancy yields a reduction of the Nusselt number Nu. However, indirectly, it can cause a simultaneous increase of the viscous dissipation and thereby Nu through a change of the flow morphology. These direct and indirect effects yield a net Nu suppression in the CC regime and a net Nu enhancement in the QC regime. In addition, we demonstrate that C^3 may provide a simplified, yet self-consistent, model system for tornadoes, hurricanes, and typhoons.

DOI: 10.1103/PhysRevLett.120.204502

Rotating turbulent thermal convection is the fundamental process underlying a variety of geo- and astrophysical flow phenomena, including deep ocean convection, planetary atmospheric flows, and liquid metal core dynamics. Rotating Rayleigh–Bénard convection (RRBC) serves as the paradigm model system; it constitutes a fluid heated from below and cooled from above that is rotated about its vertical axis. Hence, the principal external forces governing the equations of motions are the Coriolis, gravitational, and centrifugal buoyancy forces [1,2]. Traditionally, centrifugal buoyancy is disregarded in RRBC studies [3] based on the claim that it is negligible in natural settings. Exceptions exist but are mainly concerned with the onset properties [2,4–8], cf. [9] or stably stratified systems [10].

Here, we argue that centrifugal buoyancy warrants inclusion because, like gravity, it drives convective motions: Cold, denser fluid moves radially away from the axis of rotation, and warm, less dense fluid moves radially towards it. Further, it breaks the symmetry of the system and thereby changes the range of potential behaviors. Studying Coriolis-centrifugal convection (C^3)—that is RRBC with the full inertial acceleration taken into account—is also exceedingly important for today's state-of-the-art experimental devices that aim to characterize geostrophic turbulence [11]. These experiments must often rotate slower than their actual technical capabilities in order to keep the centrifugal buoyancy small. However, it is not known when centrifugal dynamics start to affect important output parameters such as the heat transport and the flow morphologies, nor in which ways those may be altered.

In this Letter, we predict the uncharted regime transitions of C^3 using scaling arguments and provide an analytical derivation for the heat transport. Our results are verified and corroborated by direct numerical simulations (DNS), which show a wide range of geophysically interesting flow behaviors.

The governing equations in nondimensional form are the incompressible Navier–Stokes equations augmented by the temperature equation, viz.,

$$D_t\boldsymbol{u} = -\boldsymbol{\nabla}p + \sqrt{\frac{\mathrm{Pr}}{\mathrm{Ra}\,\gamma^3}}\boldsymbol{\nabla}^2\boldsymbol{u} + \sqrt{\frac{\mathrm{Pr}\,\gamma}{\mathrm{Ra}\,\mathrm{Ek}^2}}\boldsymbol{u}\times\hat{\boldsymbol{e}}_z + T\hat{\boldsymbol{e}}_z - \mathrm{Fr}\,Tr\hat{\boldsymbol{e}}_r, \qquad \boldsymbol{\nabla}\cdot\boldsymbol{u} = 0, \tag{1a}$$

$$D_tT = \sqrt{\frac{1}{\mathrm{Ra}\,\mathrm{Pr}\,\gamma^3}}\boldsymbol{\nabla}^2T. \tag{1b}$$

The temperature T is scaled by the imposed adverse temperature difference Δ, lengths by the radius of the convection vessel R, velocity $\boldsymbol{u}$ by $\sqrt{g\alpha R\Delta}$, where α denotes the isobaric expansion coefficient and g is the gravitational acceleration, and time t by $R/\sqrt{g\alpha R\Delta}$, and reduced pressure p by $\rho g\alpha R\Delta$, where ρ is the mean density. The sidewall is insulated, and the top and bottom are isothermal with $T_{\mathrm{top}} = -0.5$ and $T_{\mathrm{bot}} = 0.5$, respectively. The velocity boundary conditions are no slip on all walls. The nondimensional control parameters are the Rayleigh number $\mathrm{Ra} = \alpha g\Delta H^3/(\kappa\nu)$, Prandtl number $\mathrm{Pr} = \nu/\kappa$, Ekman number $\mathrm{Ek} = \nu/(2\Omega H^2)$, Froude number $\mathrm{Fr} = \Omega^2R/g$, and aspect ratio $\gamma = R/H$, where κ is the thermal diffusivity, ν is the kinematic viscosity, Ω the rotation rate, and H is the height of the vessel.

Equations (1) are solved numerically in cylindrical coordinates (r, ϕ, z) using the fourth order finite volume code GOLDFISH [12]. In our DNS, we can independently vary Fr and the gravitational Rossby number $\mathrm{Ro}_{\parallel} \equiv \sqrt{(\mathrm{Ek}^2\mathrm{Ra}/\mathrm{Pr})}$ and even set them to 0 or ∞, respectively, while the other remains finite. This numerical flexibility, which is essential to map out the broadest possible parameter space, does not exist in the laboratory where Fr and $\mathrm{Ro}_{\parallel}$ must covary. A total number of 160 DNS are presented here, conducted with $\mathrm{Pr} = 6.52$, $\mathrm{Ra} = 10^7$ and 10^8, $0.0125 \leq \mathrm{Ro}_{\parallel} \leq \infty$, $0 \leq \mathrm{Fr} \leq 10$ in a cylindrical tank with $\gamma = 0.365$, and a small subset with $\gamma = 1.5$ [13]. Figure 1 shows characteristic flow fields for the investigated parameter space. (See the movies and Fig. 4 in the Supplemental Material [14] for a broader array of visualizations.)

We first determine when fundamental changes in the dynamics occur in the C^3 system based on time scale arguments. Relevant are the Coriolis time scale, $\tau_\Omega = 1/(2\Omega)$, the gravitational buoyancy (free-fall) time scale, $\tau_{ff} = H/\sqrt{\alpha\Delta g H}$, and the centrifugal buoyancy time scale, $\tau_{cb} = R/\sqrt{\alpha\Delta\Omega^2 R^2}$.

If the flow is three-dimensional (3D), the dynamics happen on time scales $\tau_{ff} \ll \tau_\Omega \wedge \tau_{ff} \ll \tau_{cb}$. On the other hand, if the flow is quasigeostrophic (QG), such that the primary force balance is between the pressure gradient and Coriolis forces, we have $\tau_\Omega \ll \tau_{ff} \wedge \tau_\Omega \ll \tau_{cb}$. The ratio of τ_Ω and τ_{ff} yields the gravitational Rossby number

$$\mathrm{Ro}_{\parallel} = \frac{\tau_\Omega}{\tau_{ff}} = \frac{\sqrt{\alpha g \Delta H}}{2\Omega H} = \sqrt{\frac{\mathrm{Ek}^2\mathrm{Ra}}{\mathrm{Pr}}}, \tag{2}$$

where $\parallel$ denotes the alignment of the rotation and gravitational buoyancy vectors. We estimate the transition value, $\widetilde{\mathrm{Ro}}_{\parallel}$, from 3D to QG flow using the criterion of King *et al.* [3],

$$6 \lesssim \mathrm{Pr}^{3/4}\mathrm{Ra}^{1/4}\widetilde{\mathrm{Ro}}_{\parallel}^{3/2} \lesssim 20. \tag{3}$$

This $\widetilde{\mathrm{Ro}}_{\parallel}$ transition prediction, marked by the hatched area in Fig. 2(a), works well for our Pr and Ra values and is in agreement with other studies [15].

Similarly, if the flow is quasicyclostrophic (QC), i.e., the primary force balance is between the pressure gradient and centrifugal buoyancy, the characteristic dynamical scale is $\tau_{cb} \ll \tau_\Omega \wedge \tau_{cb} \ll \tau_{ff}$. This gives a centrifugal Rossby number [16]

$$\mathrm{Ro}_{\perp} = \frac{\tau_\Omega}{\tau_{cb}} = \frac{\sqrt{\alpha\Delta}}{2} = \sqrt{\frac{\mathrm{Ek}^2\mathrm{Ra}\mathrm{Fr}}{\mathrm{Pr}\,\gamma}} = \mathrm{Ro}_{\parallel}\sqrt{\frac{\mathrm{Fr}}{\gamma}}, \tag{4}$$

where $\perp$ denotes the perpendicularity of the rotation and centrifugal buoyancy vectors. Based on the similarity of these two Rossby number definitions, we hypothesize here that the transitional $\widetilde{\mathrm{Ro}}_{\perp}$ also obeys Eq. (3), as indicated by the crosshatched area in Fig. 2(a).

We predict that the transition to centrifugally dominated flows occurs approximately where the two transition Rossby numbers are equal, corresponding to $\tau_{ff} \simeq \tau_{cb}$ [18]. Crucially, this equivalence occurs at the intersection between the $\widetilde{\mathrm{Ro}}_{\parallel}$ and $\widetilde{\mathrm{Ro}}_{\perp}$ lines in Fig. 2 when

$$\widetilde{\mathrm{Ro}}_{\parallel} \simeq \widetilde{\mathrm{Ro}}_{\perp} \quad \Leftrightarrow \quad \mathrm{Fr} \simeq \gamma. \tag{5}$$

Note, that Eq. (5) can be equivalently expressed dimensionally as $H = g/\Omega^2$, and this holds irrespective of the specific value of Eq. (3). This regime transition implies, nonintuitively, that centrifugal buoyancy effects will be strongest in low-γ vessels.

For $\mathrm{Fr} > \gamma$, there exists an important subregime where $(\tau_{cb} \sim \tau_\Omega) \ll \tau_{ff}$. It is characterized by a triple balance between pressure gradient, Coriolis, and centrifugal force (CC), which is called gradient wind balance [19].

We verify these predictions using the dimensionless heat flux, expressed by the Nusselt number Nu, that has proven to be an excellent tool to indicate regime transitions. The results presented here are for $\gamma = 0.365$; a small set of DNS with $\gamma = 1.5$ is provided in Fig. 5 of the Supplemental

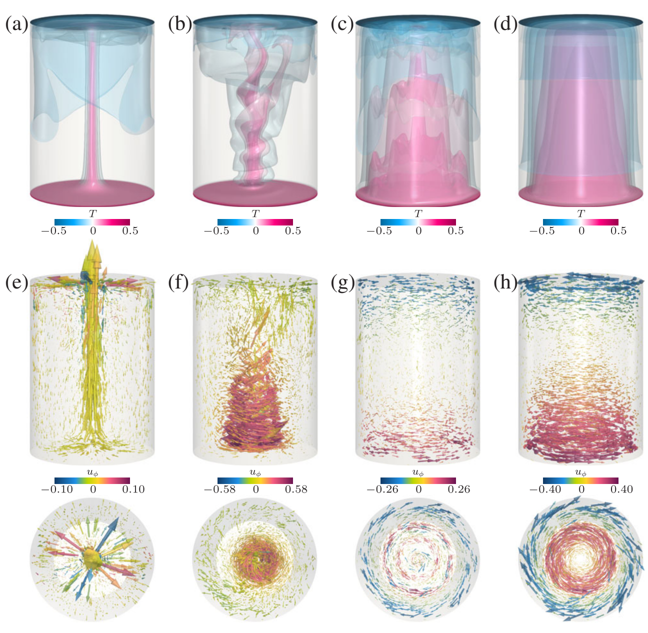

FIG. 1. Flow fields for $\mathrm{Ra} = 10^8$, $\mathrm{Pr} = 6.52$, $\gamma = 0.365$: (a–d) temperature T, (e–h) side and top view of the velocity vectors scaled in size by velocity magnitude and colored by azimuthal velocity u_ϕ. (a,e) $\mathrm{Ro}_{\parallel} = \infty$, $\mathrm{Fr} = 2.0$ (QC); (b,f) $\mathrm{Ro}_{\parallel} = 1.0$, $\mathrm{Fr} = 1.0$ (QC); (c,g) $\mathrm{Ro}_{\parallel} = 0.05$, $\mathrm{Fr} = 10.0$ (QC/CC); (d,h) $\mathrm{Ro}_{\parallel} = 0.05$, $\mathrm{Fr} = 2.0$ (CC). Note that the three rings for (h) at the top and bottom are located at approximately the same radial positions. Corresponding movies can be found in the Supplemental Material [14].

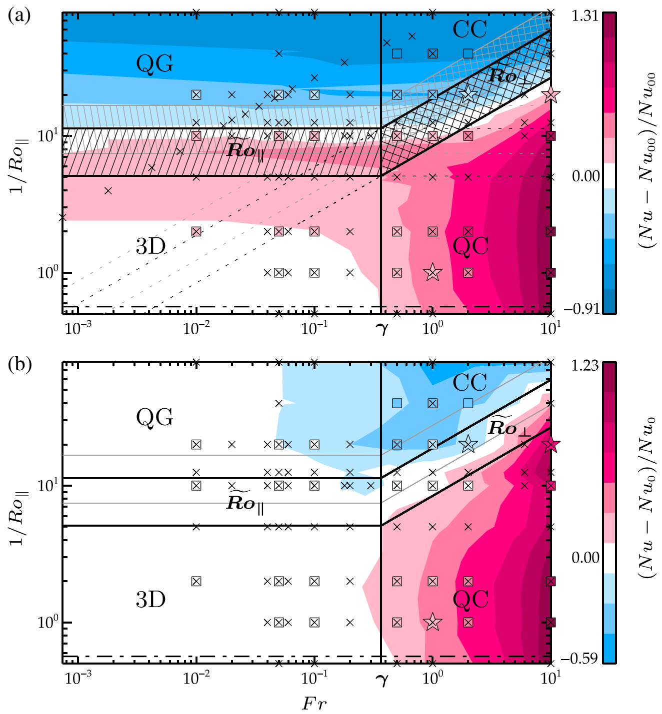

FIG. 2. Relative deviations of Nu from (a) nonrotating, noncentrifugal convection, i.e., with $\mathrm{Fr} = \mathrm{Ro}_\parallel^{-1} = 0$, and (b) traditional noncentrifugal convection, i.e., with $\mathrm{Fr} = 0$. The phase diagrams are based on the DNS conducted at $\mathrm{Ra} = 10^7$, the used data points in Fr-$\mathrm{Ro}_\parallel^{-1}$ space are marked by crosses. In addition, the color-filled symbols show the results for $\mathrm{Ra} = 10^8$ using the same color code, where the stars correspond to the cases presented in Fig. 1. The horizontal dash-dotted line indicates the bifurcation $\mathrm{Ro}_\parallel$, according to Weiss *et al.* [17]. The black (grey) hatched and crosshatched area indicate the transition region from the 3D and QC regimes to the QG and CC regimes based on $\mathrm{Ro}_\perp$ and $\mathrm{Ro}_\parallel$ for $\mathrm{Ra} = 10^7(10^8)$. The transition borders are continued with dashed lines. The vertical solid line marks $\mathrm{Fr} = \gamma$, the transition from 3D and QG to the centrifugally dominated regimes QC and CC. For clarity, hatching and dashed lines are omitted in (b).

Material [14] as supporting evidence. The relative deviation of Nu from the value without rotation $\mathrm{Nu}_{00} \equiv \mathrm{Nu}(\mathrm{Fr} = \mathrm{Ro}_\parallel^{-1} = 0)$, is shown in Fig. 2(a). Indeed, $\mathrm{Ro}_\parallel$, $\mathrm{Ro}_\perp$, and γ adequately describe the borders between different heat transfer regimes [20]. Furthermore, our regime diagram resembles those found in similarly anisotropic geophysical systems (e.g., rotating, stably-stratified dynamics described by Cushman-Roisin and Beckers [21], Fig. 11.6).

For $\mathrm{Fr} < \gamma$, the heat transport exhibits the well-known characteristics of Coriolis-affected convection at moderate Pr. With decreasing $\mathrm{Ro}_\parallel$, it is initially enhanced due to Ekman pumping in the 3D regime, and then it is suppressed due to the Taylor Proudman effect in the QG regime [3]. For $\mathrm{Fr} > \gamma$, i.e., when centrifugal buoyancy is significant, the two so-far largely unexplored QC and CC regimes show a strong heat transfer increase and decrease, respectively.

Figure 2(b) presents the relative deviation between Nu and $\mathrm{Nu}_0 \equiv \mathrm{Nu}(\mathrm{Fr} = 0)$. The quantity $(\mathrm{Nu}–\mathrm{Nu}_0)/\mathrm{Nu}_0$ differentiates the effects of Coriolis and centrifugal buoyancy forces on the heat transport. Thus, it allows us to visualize the difference in Nu between fully-inertial rotating convection ($\mathrm{Fr} \neq 0$, e.g., laboratory experiments) and cases for which centrifugal buoyancy has been omitted ($\mathrm{Fr} = 0$, e.g., idealized numerical simulations). The results in Fig. 2(b) confirm the transition prediction (5). Thus, we provide the experimentally testable prediction that a smaller γ value will not necessarily lead to weaker centrifugal effects. This differs substantively from the widespread assumption that centrifugal effects become important at a fixed estimate of $\mathrm{Fr} = 0.05$ [3,7] [e.g.], but instead, they set in earlier in low-γ vessels. Furthermore, we predict that there is an optimal Ra, according to Eq. (4), along a line of constant $\mathrm{Ro}_\perp$ for every experimental setup. Measuring along this line may allow one to map out the heat transport for arbitrary rapid rotation rates with minimal deviations due to centrifugal buoyancy effects.

To explain the contrasting effect of centrifugal buoyancy, we scalarly multiply Eq. (1) with $\boldsymbol{u}$ and average over the entire fluid volume and time. This yields the exact analytical result

$$\mathrm{Nu} = \underbrace{\frac{\mathrm{Pr}}{\gamma}\langle\|\boldsymbol{\nabla u}\|^2\rangle_{V,t}}_{\equiv \mathrm{Nu}_\varepsilon} + \underbrace{\mathrm{Fr}\sqrt{\mathrm{Pr}\,\mathrm{Ra}\gamma}\langle u_r T r\rangle_{V,t}}_{\equiv \mathrm{Nu}_{\mathrm{Fr}}} + 1. \quad (6)$$

For $\mathrm{Fr} = 0$, the well-known relationship between heat flux and viscous dissipation rate ε is recovered [22] [e.g.]. The extra term $\mathrm{Nu}_{\mathrm{Fr}}$ in Eq. (6) proves that centrifugation has a direct effect on the heat flux, which is always present. This distinguishes it from pure Coriolis convection. Furthermore, $\mathrm{Nu}_{\mathrm{Fr}}$ must be negative for sufficiently high Fr, since the hot flow is radially inwards at the bottom, i.e., $u_r < 0$ and $T > 0$, and the cold flow at the top is radially outward, $u_r > 0$ and $T < 0$. This is confirmed by the phase diagram in Fig. 3(a). The main contribution here is stemming from the boundary layers, where naturally the radial velocities and temperature anomalies are highest.

However, the other term, Nu_ε, counteracts this direct Froude effect. Thus, there is an indirect effect connected to a fundamental change in flow morphology. For $\mathrm{Ra} = 10^7$, the maximum positive contribution is almost twice as high in magnitude as the negative effect due to the centrifugality, as shown in Fig. 3(b). The reason for this is the higher ε related to stronger gradients in the velocity field, especially adjacent to the horizontal boundaries.

The flow fields presented in Fig. 1 and in the Supplemental Material [14] elucidate the fundamental changes in flow morphology in the QC and CC regimes. These visualizations show that turbulent C^3 is inherently complex, as it is susceptible to inertial, gravitational, shear, and baroclinic instabilities [4].

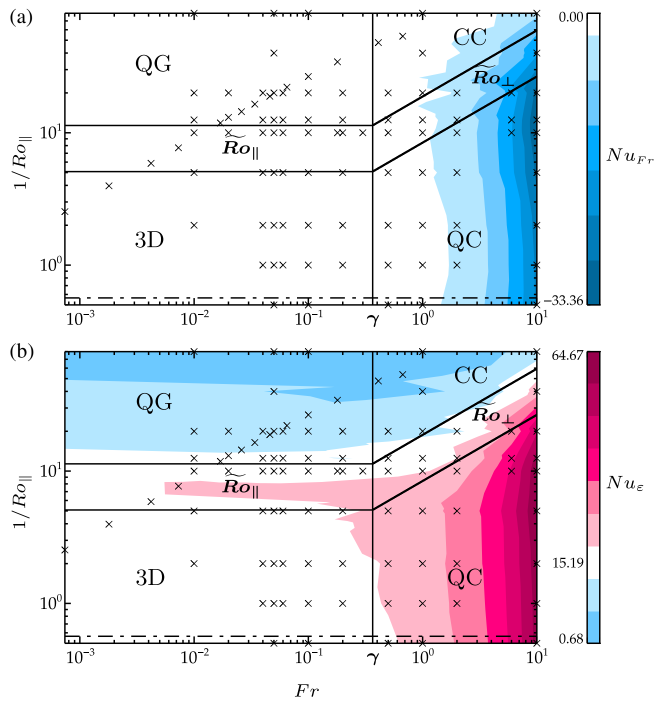

FIG. 3. Nusselt number contributions for $\mathrm{Ra} = 10^7$ according to Eq. (6); (a) $\mathrm{Nu}_{\mathrm{Fr}}$, (b) Nu_ε. The color scale is calibrated such that white corresponds to the value at $\mathrm{Fr} = \mathrm{Ro}_\parallel^{-1} = 0$. The lines mark the regime transitions and the crosses mark the Fr and $\mathrm{Ro}_\parallel^{-1}$ values of the data points used for the creation of the phase diagram, as in Fig. 2.

The most common behavior of the $\mathrm{Fr} \gtrsim \gamma$ flows is a hot central upwelling, and it is associated with the known increase of the central temperature [9,23] [e.g.]. This upwelling is visible in all flow fields in Fig. 1 and most prominently in Figs. 1(a), 1(e) for $\mathrm{Ro}_\parallel = \infty$ and $\mathrm{Fr} = 2.0$. In this case, the primary force balance is cyclostrophic (QC) and the reduced pressure is essentially parabolic in the radial direction. Even with no Coriolis force, symmetry breaking effects suffice to create a retrograde drifting vortex structure in the upper layer with an azimuthal $m = 2$ wave number.

For the other cases, $\mathrm{Ro}_\parallel$ is finite and the Coriolis force also acts on the fluid, leading to thermal winds [4,9,10,21,24]. Under the assumption of an axisymmetric, inviscid flow, and also neglecting nonlinearities and any time dependence, the C^3 thermal wind balance reads

$$\partial_z u_\phi = \mathrm{Ro}_\parallel \gamma^{-\frac{1}{2}} (\partial_r T + \mathrm{Fr}\, r \partial_z T). \qquad (7)$$

For $\mathrm{Ro}_\parallel = 1.0$ and $\mathrm{Fr} = 1.0$ [Figs. 1(b), 1(f)], the primary force balance is cyclostrophic (QC). That is, the pressure gradient and centrifugal forces dominate over the Coriolis force and the strong cyclonic (prograde) wind essentially follows the isobars. As there is a pronounced central pressure minimum where the converging hot fluid rises, the wind has a very small radius of curvature in the lower part of the cell. In addition, the upward flow is helical due to the thermal wind. In the upper part of the cell, where there is a broad pressure high, the flow diverges and becomes more three-dimensional and can even split into two warm streams. Hence, this flow is tornadolike both in appearance and in terms of the underlying physics [25].

When the Coriolis force is stronger, for $\mathrm{Ro}_\parallel = 0.05$ and $\mathrm{Fr} = 10$ [Fig. 1(c), 1(h); QC/CC], the flow speed goes down and the temperature field is steady and axisymmetric, with a conelike central hot core. The prograde azimuthal flow is strong in the lower part of the cell and connected to a pressure minimum, so that an eye in the velocity field is formed where the flow is quiescent. The retrograde circulation at the top is localized to the outer rim.

The last case, shown in Figs. 1(d), 1(h) for $\mathrm{Ro}_\parallel = 0.05$ and $\mathrm{Fr} = 2$, is in the triply balanced CC regime. There is a wide pressure high at the top; hence, the flow is anticyclonic (retrograde) and opposed to that is an equally wide pressure low at the bottom where the flow is cyclonic (prograde). This leads to a strong broadening of the temperature distribution compared to the columnar vortices found for lower Fr. Furthermore, concentric ringlike patterns are the prominent flow feature, resulting from centrifugal instabilities [26].

The last two cases demonstrate that QC and CC flows can generate eye and secondary eyewall-like structures that are qualitatively similar to those found in hurricanes and typhoons [27,28]. We, thus, argue that QC and CC flows provide new avenues for the dynamically self-consistent investigation of tornado and tropical cyclone physics.

In sum, our results have substantial implications for the investigation of rotating convection systems. They suggest that the geometry of the tank is crucial to determine the particular regime of Coriolis-centrifugal convection. We make the testable prediction that the transition to centrifugally dominated convection occurs when $\mathrm{Fr} \gtrsim \gamma$, instead of a fixed absolute Fr value as traditionally assumed. In future laboratory and numerical studies, we will further vary γ and make use of other diagnostic tools such as the center temperature [9,15,23].

We thank E. K. Hawkins, E. M. King and J. C. McWilliams for Froude-ful discussions and two anonymous referees for their constructive feedback. S. H. acknowledges funding by the Deutsche Forschungsgemeinschaft (DFG) under Grant No. HO 5890/1-1. We thank the NSF Geophysics Program for financial support through Grant No. 1547269. We also gratefully acknowledge the Leibniz-Rechenzentrum for providing computational resources on SuperMUC.

*susannehorn@ucla.edu

[1] S. Chandrasekhar, *Hydrodynamic and Hydromagnetic Stability* (Clarendon Press, Oxford, 1961).
[2] F. Marques, I. Mercader, O. Batiste, and J. M. Lopez, J. Fluid Mech. **580**, 303 (2007).

[3] K. Julien, S. Legg, J. McWilliams, and J. Werne, J. Fluid Mech. **322**, 243 (1996); J.-Q. Zhong, R. J. A. M. Stevens, H. J. H. Clercx, R. Verzicco, D. Lohse, and G. Ahlers, Phys. Rev. Lett. **102**, 044502 (2009); R. J. A. M. Stevens, J.-Q. Zhong, H. J. H. Clercx, G. Ahlers, and D. Lohse, Phys. Rev. Lett. **103**, 024503 (2009); E. M. King, S. Stellmach, and J. M. Aurnou, J. Fluid Mech. **691**, 568 (2012); R. P. J. Kunnen, R. J. A. M. Stevens, J. Overkamp, C. Sun, G. F. van Heijst, and H. J. H. Clercx, J. Fluid Mech. **688**, 422 (2011); R. E. Ecke and J. J. Niemela, Phys. Rev. Lett. **113**, 114301 (2014); S. Horn and O. Shishkina, J. Fluid Mech. **762**, 232 (2015); S. Horn and P. J. Schmid, J. Fluid Mech. **831**, 182 (2017).

[4] M. A. Torrest and J. L. Hudson, Appl. Sci. Res. **29**, 273 (1974); G. M. Homsy and J. L. Hudson, J. Fluid Mech. **48**, 605 (1971).

[5] J. M. Lopez, A. Rubio, and F. Marques, J. Fluid Mech. **569**, 331 (2006).

[6] J. Lopez and F. Marques, J. Fluid Mech. **628**, 269 (2009).

[7] J. Curbelo, J. M. Lopez, A. M. Mancho, and F. Marques, Phys. Rev. E **89**, 013019 (2014).

[8] N. Becker, J. D. Scheel, M. C. Cross, and G. Ahlers, Phys. Rev. E **73**, 066309 (2006).

[9] J. Hart and D. Ohlsen, Phys. Fluids **11**, 2101 (1999); J. E. Hart, J. Fluid Mech. **403**, 133 (2000).

[10] V. Barcilon and J. Pedlosky, J. Fluid Mech. **29**, 673 (1967); G. M. Homsy and J. L. Hudson, J. Fluid Mech. **35**, 33 (1969); N. Brummell, J. E. Hart, and J. M. Lopez, Theor. Comput. Fluid Dyn. **14**, 39 (2000).

[11] J. S. Cheng, J. M. Aurnou, K. Julien, and R. P. J. Kunnen, Geophys. Astrophys. Fluid Dyn., arXiv:1703.02895; J. M. Aurnou, M. A. Calkins, J. S. Cheng, K. Julien, E. M. King, D. Nieves, K. M. Soderlund, and S. Stellmach, Phys. Earth Planet. Inter. **246**, 52 (2015); S. Stellmach, M. Lischper, K. Julien, G. Vasil, J. S. Cheng, A. Ribeiro, E. M. King, and J. M. Aurnou, Phys. Rev. Lett. **113**, 254501 (2014); R. P. J. Kunnen, R. Ostilla-Mónico, E. P. van der Poel, R. Verzicco, and D. Lohse, J. Fluid Mech. **799**, 413 (2016).

[12] O. Shishkina, S. Horn, S. Wagner, and E. S. C. Ching, Phys. Rev. Lett. **114**, 114302 (2015); O. Shishkina and S. Horn, J. Fluid Mech. **790**, R3 (2016).

[13] These parameters are chosen to foster comparison with upcoming experiments using UCLA's NoMag device (https://youtu.be/Et6mnyn9PzE).

[14] See Supplemental Material at http://link.aps.org/supplemental/10.1103/PhysRevLett.120.204502 for movies, a broader array of visualizations, and additional analyses for the $\gamma = 1.5$ cases.

[15] S. Horn and O. Shishkina, Phys. Fluids **26**, 055111 (2014).

[16] The square-root of $\mathrm{Ro}_\perp$ is also called the density deficit parameter or the thermal Rossby number [9,10].

[17] S. Weiss, R. J. A. M. Stevens, J.-Q. Zhong, H. J. H. Clercx, D. Lohse, and G. Ahlers, Phys. Rev. Lett. **105**, 224501 (2010).

[18] This is not expected to be a first order transition, and instead occurs over a relatively broad range centered in the vicinity of $\widetilde{\mathrm{Ro}}_\perp \simeq \widetilde{\mathrm{Ro}}_\parallel$.

[19] H. E. Willoughby, J. Atmos. Sci. **47**, 265 (1990).

[20] We also indicate where the flow starts to be mildly affected by the Coriolis force according to Weiss *et al.* [17], noting that this holds for almost all of our results.

[21] B. Cushman-Roisin and J.-M. Beckers, *Introduction to Geophysical Fluid Dynamics: Physical and Numerical Aspects* (Academic Press, New York, 2011), Vol. 101.

[22] B. I. Shraiman and E. D. Siggia, Phys. Rev. A **42**, 3650 (1990); S. Grossmann and D. Lohse, J. Fluid Mech. **407**, 27 (2000).

[23] Y. Liu and R. E. Ecke, Phys. Rev. E **84**, 016311 (2011).

[24] J. M. Aurnou, S. Andreadis, L. Zhu, and P. Olson, Earth Planet. Sci. Lett. **212**, 119 (2003).

[25] R. Rotunno, Annu. Rev. Fluid Mech. **45**, 59 (2013); R. Rotunno, G. H. Bryan, D. S. Nolan, and N. A. Dahl, J. Atmos. Sci. **73**, 3843 (2016); B. H. Fiedler, Q. J. R. Meteorol. Soc. **124**, 2377 (1998).

[26] E. L. Koschmieder, Beitr. Phys. Atmos. **40**, 216 (1967).

[27] M. T. Montgomery and R. K. Smith, Annu. Rev. Fluid Mech. **49**, 541 (2017).

[28] S. Nong and K. Emanuel, Q. J. R. Meteorol. Soc. **129**, 3323 (2003).

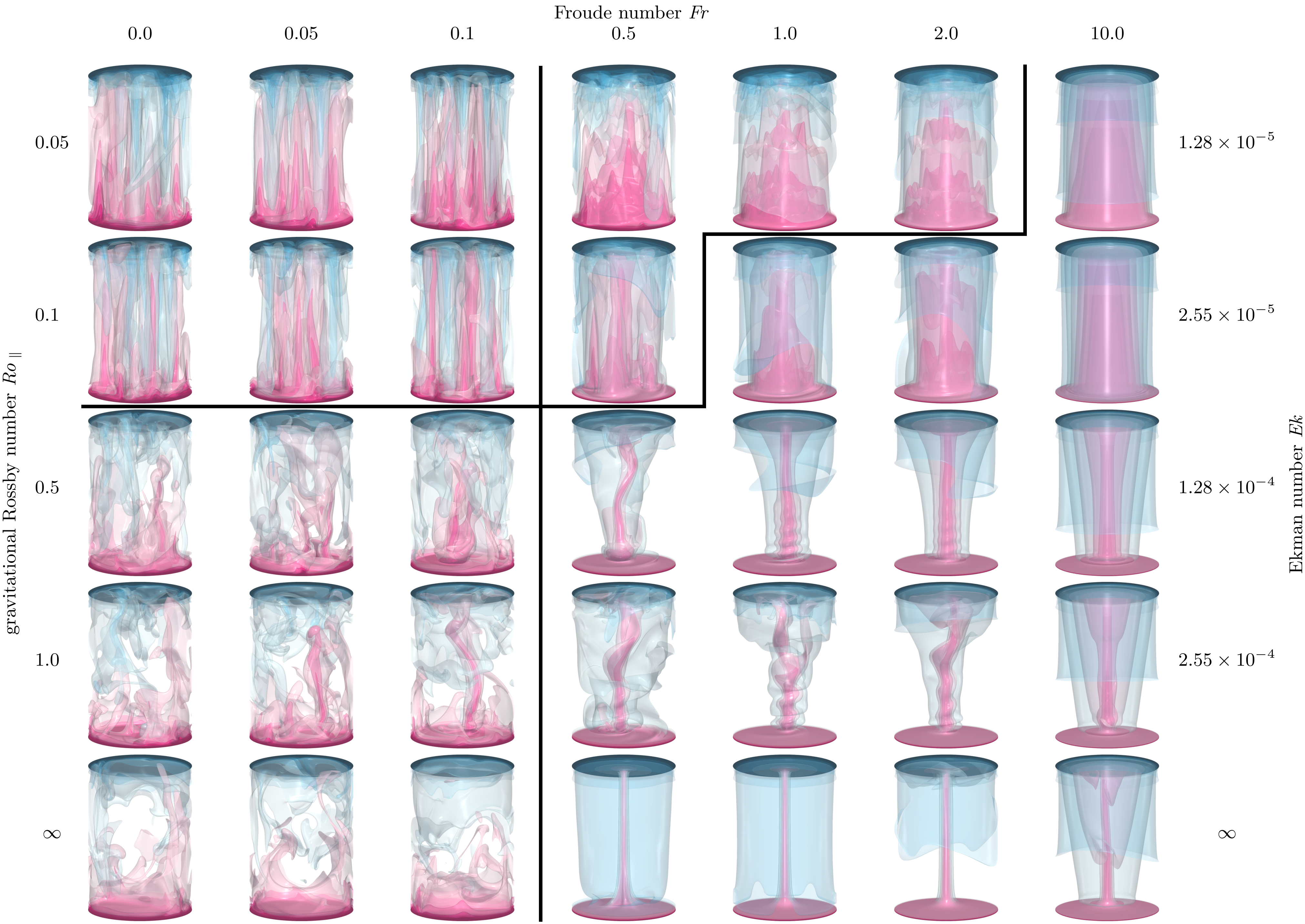

Froude number Fr
0.0
0.05
0.1
0.5
1.0
2.0
10.0
gravitational Rossby number $Ro_{\parallel}$
0.05
0.1
0.5
1.0
∞
Ekman number Ek
1.28×10^{-5}
2.55×10^{-5}
1.28×10^{-4}
2.55×10^{-4}
∞

FIG. 4. Supplemental figure to Fig. 1. Shown are ten temperature isosurfaces for $Ra = 10^8$, equidistantly distributed between the top and bottom temperature. The lines mark the regime transitions as in Fig. 2. Note, that the transition range is relatively broad, thus, flow fields close to the borders exhibit also minor signatures of the adjacent regime(s).

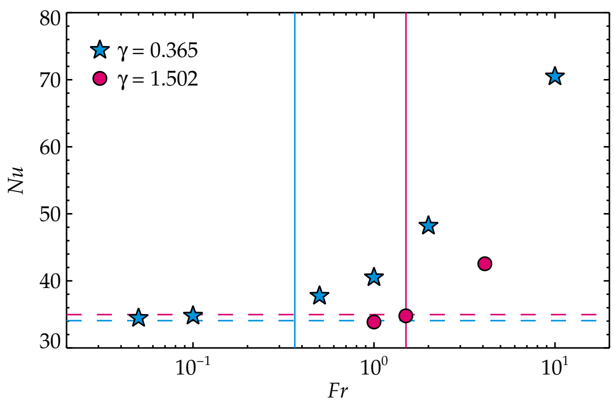

FIG. 5. Nusselt number Nu as function of the Froude number Fr for $Ra = 10^8$ and $Ro = 1.0$. The blue stars and lines correspond to $\gamma = 0.365$, presented in the main part of the Letter. The magenta circles and lines correspond to additional simulations conducted at a higher aspect ratio of $\gamma = 1.502$ for $Fr \in \{0, 1.0, 1.5, 4.1\}$. The horizontal dashed lines mark $Nu(Fr = 0)$ and the vertical solid lines the predicted transition at $Fr = \gamma$.